Solar Energy Materials & Solar Cells 123 (2014) 41–46

Contents lists available at ScienceDirect

Solar Energy Materials & Solar Cells

journal homepage: www.elsevier.com/locate/solmat

Improved local efficiency imaging via photoluminescence for silicon solar cells

Chao Shen [a,*], Martin A. Green [a], Otwin Breitenstein [b], Thorsten Trupke [a], Muye Zhang [a], Henner Kampwerth [a]

[a] University of New South Wales, Sydney, NSW 2036, Australia
[b] Max Planck Institute of Microstructure Physics, Weinberg 2, D-06120 Halle, Germany

ARTICLE INFO

Article history:
Received 24 June 2013
Received in revised form
2 January 2014
Accepted 2 January 2014

Keywords:
Efficiency
Imaging
Photoluminescence
Solar cell
Spatially resolved
Silicon

ABSTRACT

We present an improved method that uses photoluminescence images to calculate the spatially-resolved efficiency in addition to other performance parameters of silicon solar cells. This new method is simpler than our previously-presented two-diode method, using only one diode with a variable ideality factor. Experimental results show that the simplified method is more tolerant of very large variations in local series resistance, a characteristic commonly seen in silicon cells. Using dark lock-in thermography techniques, we quantitatively verify the efficiency images produced by our improved method.

1. Introduction

The measurement of solar cell efficiency has previously been limited to a determination of the terminal characteristics of the cell, which represent an average of the spatially-varying properties of the device. Spatially-resolved efficiency images recently became available with the work of Shen et al. [1], led by the work of Glatthaar et al. [2]. Simultaneously, Breitenstein [3] published a technique based on dark lock-in thermography (DLIT) that calculated an efficiency image incorporating shunt influence, whereas Shen [1] did not include this explicitly. After Shen et al. [4] validated their results qualitatively with CELLO measurements [5], Shen′s and Breitenstein′s methods were compared [6]. The comparison showed that Shen′s efficiency image was incorrectly affected by high series resistance (R_s) impact on the dark saturation current of the second diode J_{02}. Inspired by Glatthaar et al. [2] again, we present an improved method based on [1,2] to generate a set of images that show increased accuracy around the maximum power point of the cell. The images are inherently self-consistent and appear to have overcome the previous problems of the R_s influence on other parameters [6]. This paper introduces the theory in Section 2, the calculated images in Section 3 and a comparison and discussion in Section 4.

2. Theory

Our algorithm uses a minimum of four photoluminescence (PL) images at different electrical bias and illumination conditions as inputs. The output images are the calibration constant C_{xy}, series resistance $R_{s,xy}$, the local voltage $V_{oc,xy}$ at a terminal open circuit, the local voltage $V_{mpp,xy}$ at a terminal maximum power point (MPP), the local current density $J_{mpp,xy}$ at the terminal MPP, dark saturation current density $J_{0,xy}$, and power density P_{xy} or, equivalently, efficiency η_{xy}. In this context, the subscripts xy are the coordinates of a pixel on the CCD camera, which define a "point" on the cell.

The equations are similar to those used in our previous work [4]. The commonly accepted correlations between the luminescence photon flux $\phi_{PL,xy}$ (i.e., the PL images) and the local voltage V_{xy} [7,8] are shown in Eqs. (1) and (2a). C_{xy} is a calibration constant containing unknown optical parameters and other scaling constants. It is assumed to be independent of electrical bias and illumination conditions. Eq. (2a) calculates the net PL photon flux $\phi_{net,xy}$ that is used in Eq. (1). Eq. (2b) depicts Glatthaar′s [2] approximation that only one image $\phi_{offset,xy,1sun}$ at short circuit and one sun illumination condition are required to determine the offset photon flux $\phi_{offset,xy}$. This flux is primarily caused by diffusion-limited carrier recombination [7]. To calculate $\phi_{offset,xy}$ at different illumination intensities, a scaling factor β_{sun} is used. For example, for half-sun intensity, β_{sun} is 0.5. The thermal voltage V_T is kT/q, where k is Boltzmann′s constant, T is the cell

* Corresponding author. Tel.: +61 433666505.
E-mail address: hunterchaoshen@gmail.com (C. Shen).

0927-0248/$ - see front matter
http://dx.doi.org/10.1016/j.solmat.2014.01.003

temperature and q is the charge of an electron. The local current density J_{xy} is defined by the Shockley diode equation [9] with a single ideality factor n and light-generated current density J_{light}; see Eq. (3). This parameter is assumed to be uniform throughout the cell and equals the short circuit current density. This assumption is common to most of the PL imaging techniques, but still remains controversial. The ideality factor n is also assumed to be uniform across the cell. However, the local variations in efficiency caused by diode properties will still be reflected by variations in $J_{0,xy}$. Therefore, the dark current will be reasonably correct. Eq. (4) describes the current density J_{xy}, which is defined by the voltage drop between the local voltage V_{xy} and terminal voltage V_{term} through the local series resistance $R_{s,xy}$. J_{xy} is therefore the local current density that contributes to the terminal current.

$$V_{xy} = V_T \ln\left(\frac{\phi_{net,xy}}{C_{xy}}\right) \tag{1}$$

$$\phi_{net,xy} = \phi_{PL,xy} - \phi_{offset,xy} \tag{2a}$$

$$\phi_{offset,xy} = \beta_{sun}\phi_{offset,xy,1sun} \tag{2b}$$

$$J_{xy} = -J_{0,xy}(e^{(V_{xy}/nV_T)} - 1) + J_{light} \tag{3}$$

$$J_{xy} = \frac{V_{xy} - V_{term}}{R_{s,xy}} \tag{4}$$

Eq. (5) is obtained by combining Eqs. (1), (3) and (4):

$$\underbrace{V_T \cdot \ln(\phi_{net,xy}) - V_{term}}_{a_{xy}} = \underbrace{V_T \ln C_{xy}}_{X_{xy}} + \underbrace{R_{s,xy} J_{light}}_{Y_{xy}\ b_{xy}} - \underbrace{\frac{J_{0,xy}R_{s,xy}}{\sqrt[n]{C_{xy}}}}_{Z_{xy}} \underbrace{\sqrt[n]{\phi_{net,xy}}}_{C_{xy}} \tag{5}$$

2.1. Calculation

The calculation consists of eight steps and is summarized in two stages A and B, described in the flow chart in Fig. 1.

Stage A. The first stage is to find a global ideality factor n and condition independent images C_{xy}, $R_{s,xy}$ and $J_{0,xy}$. The ideality factor n is assumed to be uniform across the cell and calculated via an iterative loop. For example, an initial value of $n=1.2$ (illuminated) may be assumed. Then steps 2–5 are repeated until the averaged current density J_{xy} of each point matches the measured global current density J_{global} at the maximum power point. In this case the calculated global ideality factor n and condition-independent images C_{xy}, $R_{s,xy}$ and $J_{0,xy}$ will be passed on to stage B. Although the assumption of a uniform ideality factor does not distinguish the diode feature of each point (into J_{01} or J_{02} described in [4]), the overall diode properties will still be reflected in $J_{0,xy}$ as well as the overall recombination current (the first term in Eq. (3)). Hence, the overall efficiency will still be sensitive to individual local diode properties. The efficiency image will be reasonably correct because at a particular point (MPP), only the current density is used to calculate the efficiency, and the current density relies on the combination of $J_{0,xy}$ and n instead of only n; see Eq. (3). In addition, since the average calculated current density is always equal to the global current density, the efficiency map is more adaptable to cells with large R_s variation according to our experiments.

In step 3, sections of the upper expression in Eq. (5) are substituted into known parameters a_{xy}, b_{xy} and c_{xy} and unknown parameters X_{xy}, Y_{xy}, and Z_{xy}. Each PL image, identified by an index i, will generate one set of variables $a_{i,xy}$, $b_{i,xy}$ and $c_{i,xy}$. These can be seen as a coordinate triplet in a three-dimensional space. All images will generate points in this space. A least-square-fit-based linear

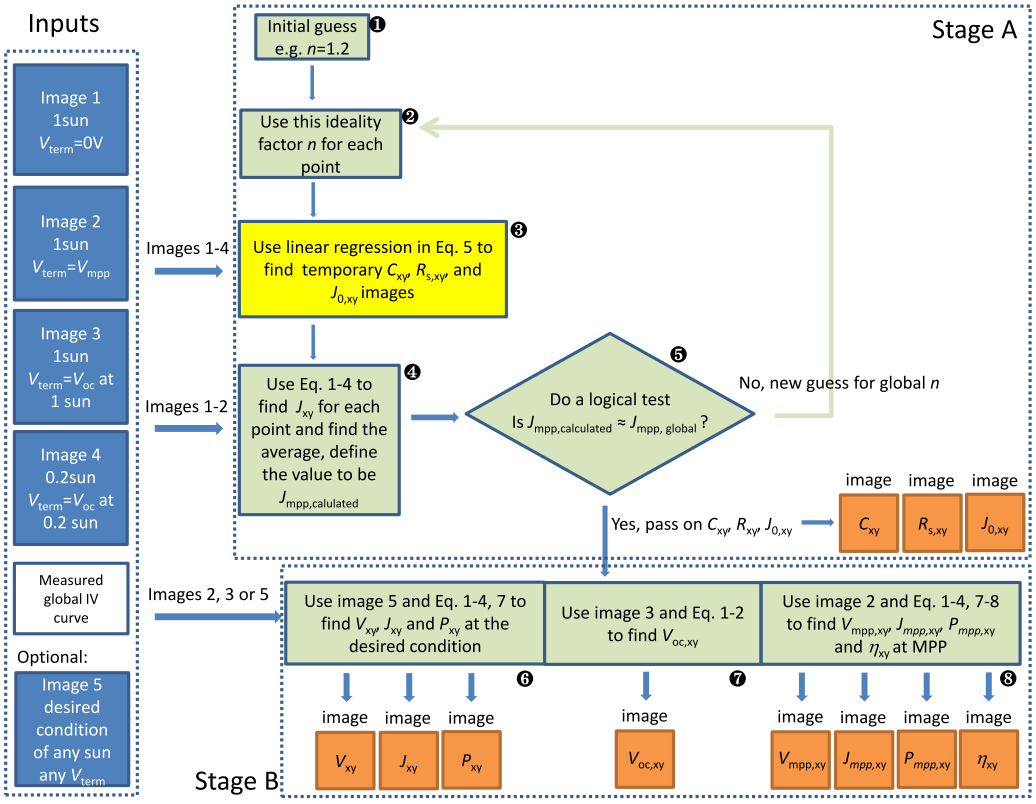

Fig. 1. The schematic flow chart of the algorithm. It has two stages. Eight individual steps are marked with black circled numbers. Blue images represent input images and orange images represent output images. The main calculation step is step 3, which is marked in yellow. Note that in stage B, the OC and MPP means that the terminal voltage is at open circuit and maximum power point condition.

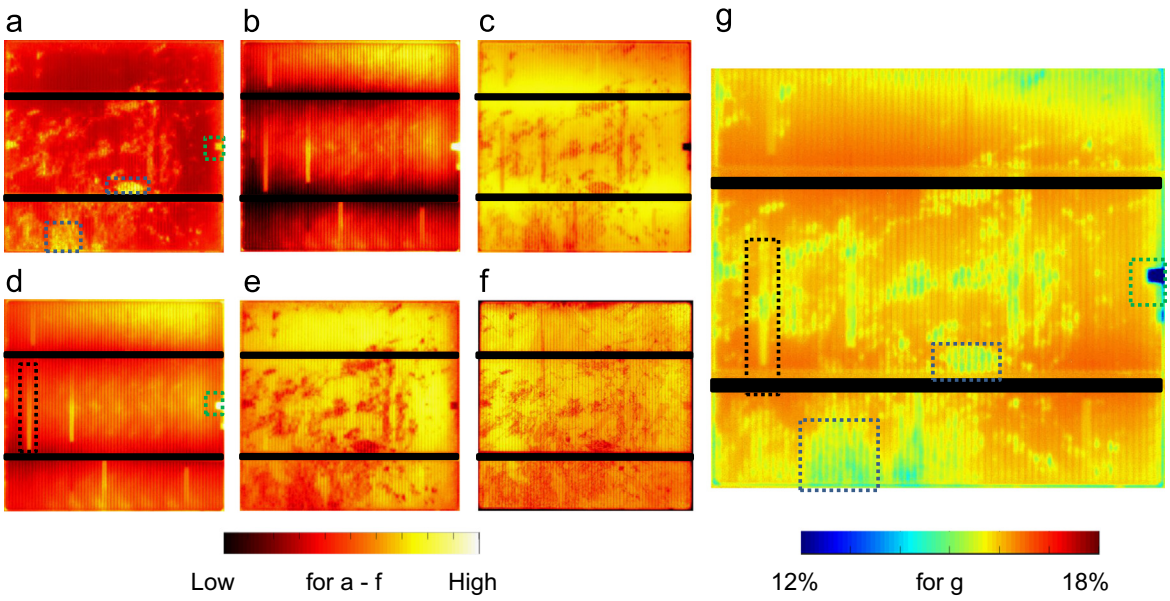

Fig. 2. Calculated images. (a) Dark saturation current density J_0 at ideality factor $n=1.15$, with scale $0–10^{-10}$ A/cm^2. (b) Maximum power point voltage V_{mpp}, with scale 520–560 mV. (c) Maximum power point current density J_{mpp}, with scale 25–35 mA/cm^2. (d) Series resistance R_s, with scale 0–2 Ω cm^2. (e) Open circuit voltage V_{oc}, with scale 590–625 mV. (f) Calibration constant C, with scale 2×10^{-7}–10^{-8}. In our experience, a higher C value usually implies a higher bulk lifetime, but this remains to be proved. (g) Efficiency image scaled to clearly distinguish efficiency values. The same image in a monotonic scale system will be shown in the next section. Busbar resistances are neglected since probes are evenly spring loaded to busbars.

regression will then find the most agreeable line for all the points, which is then expressed by the triplet (X_{xy}, Y_{xy}, Z_{xy}). The number of input PL images is therefore flexible, as long as more than four images are used. These include an image to calculate net photon flux $\phi_{net,xy}$ in Eq. (2) and three images at different electrical bias and illumination intensity conditions for the 3D linear fit. A higher number of input images will reduce the resulting uncertainty and noise of the final output parameters, for example, more illumination conditions, and more bias conditions.

Once the unknown X_{xy}, Y_{xy}, and Z_{xy} are found, the cell's parameters can be calculated by the substitutions made in the lower line of Eq. (5):

$$C_{xy} = e^{(X_{xy}/V_T)} \tag{6a}$$

$$R_{s,xy} = Y_{xy} \tag{6b}$$

$$J_{0,xy} = Z_{xy} \cdot \frac{\sqrt[n]{C_{xy}}}{Y_{xy}} \tag{6c}$$

Stage B. The parameters found in stage A are assumed to be independent of the electrical bias and illumination conditions, whereas local voltage V_{xy}, current density J_{xy}, and power density P_{xy} are not. In this stage, these parameters can be calculated for an arbitrary operating condition, described in parallel steps 6–8. For this, a PL image at this desired condition can be used (this image can be one of the original input images of stage A if the operation condition is suitable). For example, a voltage image $V_{oc,xy}$ at the terminal open circuit is calculated via Eqs. (1), (2a) and (2b) by using a PL image at one-sun illumination and terminal open circuit conditions. The local current density J_{xy} and effective power density P_{xy} can be calculated via Eqs. (3) and (7) respectively.

$$P_{xy} = V_{term} J_{xy} \tag{7}$$

The power density map P_{xy} in mW/cm^2 can also be read as an efficiency map η_{xy} if the terminal MPP condition is used and it is normalized to the illumination power density P_{light}:

$$\eta_{xy} = left.\frac{P_{xy}}{P_{light}}\right|_{MPP} \tag{8}$$

One difference between this and Glatthaar's [2] procedures is that we use a single global variable ideality factor n to fit the result to the terminal I–V characteristics, which is supported by injection-dependent lifetime theory [10] in some degree. In addition, we calculate efficiency images.

3. Calculated images

The following images are calculated from PL images taken by a commercial BT Imaging LIS-R1PL imaging system [11]. The conditions are given in the caption of Fig. 1. Images 2–4 in Fig. 1 can also be chosen from 490 mV to 700 mV terminal voltage and 0.2 to 1 sun illumination. Please also note that for input image 4, 0.2 sun is selected only for a good balance between laser stability and regression accuracy. In fact, a different combination of input image selections might produce even more accurate results of the efficiency image. All displayed images are from the same multicrystalline solar cell, which was also used in [6].

Fig. 2 shows the calculated images. The dark saturation current density J_0 in Fig. 2a describes the recombination characteristics. High J_0 regions such as grain boundaries have high recombination and reduced efficiency: see the blue and green boxed regions in Fig. 2a and g. As the ideality factor n is not 1 or 2, separation of bulk and junction recombination is difficult. The R_s image, Fig. 2d, shows the series resistance between each point and the cell terminals, and the definition of local series resistance is described in more detail in [12]. For this solar cell, broken fingers (for example, those highlighted by the black box) cause a reduction in efficiency; see Fig. 2g. The region indicated by the green box on the right hand side has no metal back contact. It lacks surface passivation and has therefore both high R_s and surface recombination. In summary, both are reflected as a significant efficiency drop in Fig. 2g. The distribution of the simultaneously calculated local calibration constant C in Fig. 2f is only required for Eq. (1). It is an essential parameter to link the electrical signal (local voltage V_{xy}) to the optical signal (luminescence $\phi_{net,xy}$). Fig. 2b and e shows the local voltage images with the terminals at the MPP and open circuit respectively. Fig. 2c shows the current density J_{mpp} map

that shows the current contribution from each point of the cell at terminal MPP. The efficiency image in Fig. 2g presents the overall performance of the solar cell. In summary, this sample is affected by four efficiency-reducing phenomena: (1) broken fingers (black box in g), (2) grain boundaries (blue boxes in g), (3) no back contact region (green box in g), and (4) regions that are far from the busbars. (It can be seen from d and g that regions far from busbar general have higher series resistance and hence lower efficiency.) Note that the last one is not a defect but a shortcoming of grid design because current produced from those regions must travel a relatively long distance through the fingers. For example, a three-busbar cell will demonstrate less efficiency reduction but will incur other efficiency-reducing nonidealities.

4. Comparison with DLIT and light *I–V* measurement and discussion

4.1. Comparison

For verification of features and values, we compare our efficiency image to the DLIT-based technique [3], as shown in Fig. 3. Both are presented in the same color scale. Although they are based on two completely different approaches and technologies, the results are nearly identical. A noticeable difference is a circular region near the top edge of the cell and some small points on the bottom edge. They are likely caused by shunting underneath the fingers [13] and edge shunts respectively, which cannot be detected by our new method but can be identified by DLIT.

Both methods offer high spatial resolution, non-destructiveness, and quantitative results. This new method operates under illumination, whereas the DLIT-based method operates in dark. Compared to the DLIT-based efficiency image, the new PL-based image does not offer J_{01} and J_{02} during its calculation. It also does not detect weak ohmic shunts, which can be measured by DLIT. However, the DLIT efficiency image may be disturbed by large R_s values ($>3\ \Omega\,\mathrm{cm}^2$) and thermal blurring, whereas this PL-based technique seems robust to these effects [6]. The new PL-based method could be incorporated into existing PL systems simply via a software update and will result in an overall measurement time of a few minutes.

Fig. 4 shows a comparison of calculated and directly-measured global *I–V* curves. The blue curve with diamonds was calculated by summing up all local currents for selected terminal voltages. In principle, a shunted cell cannot be measured by this method because PL images are only weakly sensitive to shunts that occur underneath metallized regions [13]. To give a comparison nevertheless, the calculated curve is slightly shifted downwards by subtracting the leaked current. Region C shows some mismatches. This might be explained by the neglecting of the injection-dependent ideality factor [19]. When the voltage increases, for example from MPP to OC, the ideality factor also increases. Then the calculated curve in region C should bend downwards more and locate closer to the measured curve. It may also be explained by the simplification of having a voltage-independent $R_{s,xy}$ [14], the neglecting of any cross-current flow between points on the cell [15] and the use of the one-diode equation, which naturally describes only a limited voltage range. However, in general, the data matches well in region A and particularly in region B (near the MPP), which is especially important for producing the efficiency image.

4.2. Discussion

Compared to our previous two-diode method [4], this new method simplifies the model to one diode with the variable ideality factor n. According to our experiments, the previously-

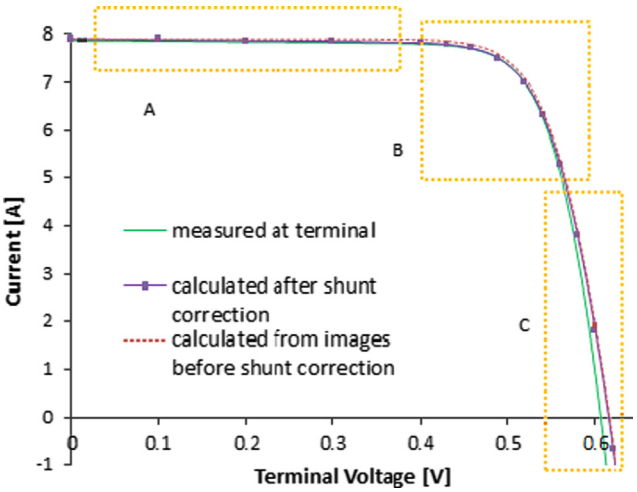

Fig. 4. Comparison of directly-measured, calculated and shunt corrected terminal characteristics. After slight shunt correction, the two solid lines can be compared. Ideally, they should overlap each other. The two curves match well, except in region C.

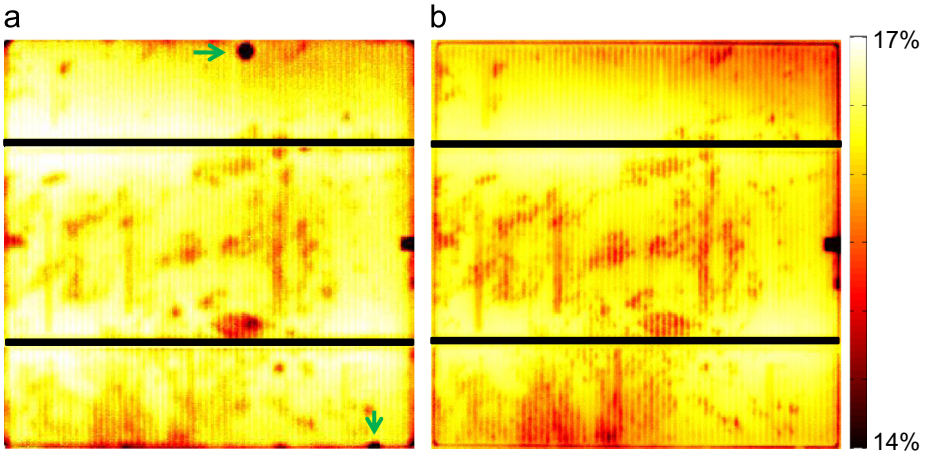

Fig. 3. Comparison between the DLIT-based (a) and the proposed PL-based (b) efficiency images. They appear very similar. Note that both maps are calibrated to the same illumination light intensity, and the measured efficiency is based on the active region only. If busbars are considered, the efficiency value should be multiplied by a factor of 0.962.

developed method [4] is able to separate J_0 into J_{01} and J_{02}, whereas the new method produces an efficiency image with less error. The new method also produces more robust results when analyzing cells with large variation in series resistance. For example, for some cells, a broken finger area does not always demonstrate a visible efficiency drop in the image calculated by the old method. However, the new method always shows a visible efficiency drop, as can be seen in Fig. 3.

The reasoning behind this observation merits a brief discussion. Both our models and some other PL imaging publications oversimplify the real situation for the current path in the cell. Consider first a good point on the cell. Current is assumed to flow from this good point firstly to the finger and then to the terminal through a certain series resistance $R_{s,1}$. Taking then a bad point on the cell, current is assumed to flow from the terminal through the finger to this point through a certain series resistance $R_{s,2}$. Then, current redistribution from the good point to the bad point will encounter $R_{s,1}+R_{s,2}$. This could be a reasonable description if these two points are far away from each other, but will be incorrect if these two points are close to each other. In that case, the current will take the shortest path from the good point to the bad point directly through smaller R_s. Moreover, it is well known that R_s is not strictly constant. Instead, the most prominent contributions to R_s, the lateral sheet resistance of the emitter and the grid line resistances, are the so-called distributed resistances, as described in [16,17]. Simplifications that overlook these phenomena will lead to an R_s error.

Unfortunately, R_s plays a decisive role in many PL evaluation techniques, including that described in [4] and this new method. For a cell with no R_s variations, the error will be insignificant, and both methods should produce correct results. For a cell with R_s variations, which is the real situation, the R_s error varies to a greater or lesser extent. Hence, strictly speaking, all PL-based methods that use these kinds of current path and constant R_s assumptions are incorrect. However, approximations can be made if the method is less disturbed by the errors incurred in these assumptions. Our experimental results show that the two-diode model is more sensitive to the R_s error than the one-diode model. This is because J_{02} in Eq. (5) in [4] is distinguished by a square root dependency on the net photon flux. Compared to the variable term c_{xy} to determine J_{01}, the range of the variable term d_{xy} is too small. Errors in estimating J_{02} will have a large impact on the efficiency. Therefore, the one-diode model with the ideality factor n is more adaptable to R_s variations [16].

4.3. Limitations of the method

Despite the improvements seen in quantitative results produced by this new method, several important limitations remain. First, the method is still affected by the R_s measurement error, and for a cell with R_s out of the range 0.3–5 Ω cm^2, the results may be unreliable. Second, this method uses biased PL images as inputs. This method is still unsuitable for cells that cannot be properly measured by PL: for example, it cannot characterize cells with topside glass layers. From our experiments, this new method worked well for conventional commercial front contacted Al-BSF Si solar cells, metal plated Si cells, laser doped selective emitter cells, thin silicon rear-junction n-type cells, and semiconductor finger Si cells. This method might also work for passivated emitter rear cells and interdigitated back contact cells, but a different interpretation of the result might be required. However, for non-silicon cells, the PL system setup should be modified, at least with regard to the filters in front of the laser and camera. It may not work properly for cells with more than one p–n junction or if a point on the cell cannot represent a stack of layers (e.g. double sided cells and sliver cells). Significantly-shunted cells also cannot be analyzed by this method.

Note that we assumed uniform light-generated current J_{light} across the cell. For a cell with large variations in J_{light}, this method will not work well. It may be possible to use the method of Padilla et al. [18] to find local J_{light} to improve the accuracy of this new method for such a case, but this might complicate the experimental setup and increase the measurement time. By adapting a faster and simpler J_{light} imaging method in the future, the b_{xy} term in Eq. (5) can be replaced with a $J_{light,xy}$ image. Then, this limitation can be removed.

Similarly, we assumed a uniform ideality factor for the entire cell to enable the calculation. For cells with large variations in the ideality factor, the accuracy will be decreased. Hameiri et al. [19] proposed a PL-based ideality factor imaging method. However, internal balancing/circulating current is neglected during the ideality factor imaging, which makes this method controversial. If this ideality factor imaging method is improved in the future, steps 1, 2, 4 and 5 in Fig. 1 can be simply replaced by an ideality factor image. Then, this limitation can be removed.

Finally, it bears noting that the overall measurement takes several minutes, making this improved method inappropriate for inline applications. Futhermore, proper hardware support is essential. For example, the cell has to be evenly and properly contacted with the chuck and the probes when it is voltage-biased. Small non-uniformities caused by hardware might lead to large errors.

5. Conclusion

A new algorithm is presented to calculate local solar cell efficiency, together with five other parameters from PL images. A minimum of four PL images can be used as inputs, whereas more and better selections of the images will reduce residual noise. Comparison with a DLIT-based technique [3] shows a good agreement between these two very different methods, which underlines the validity of both. Furthermore, the locally-calculated currents are compared to the measured terminal I-V characteristic with good agreement at the maximum power point. Unlike our previous work [4], this new method does not provide dark saturation current densities J_{01} and J_{02}. However, from the first trials with different samples, the results of this new technique appear less disturbed by large variations in series resistance. The limitations of this method are also listed, but by adapting appropriate light-generated current and ideality factor imaging methods in the future, two major limitations can be removed and the accuracy will be significantly increased. Based on our experience, at least 60% of the cells in the market can use this method to acquire a reasonably reliable quantitative efficiency image.

Acknowledgment

This Program has been supported by the Australian Government through the Australian Renewable Energy Agency (ARENA). Responsibility for the views, information or advice expressed herein are not accepted by the Australian Government. The English correction from Craig Johnson was also greatly appreciated.

References

[1] C. Shen, H. Kampwerth, M.A. Green, Spatially resolved photoluminescence imaging of essential silicon solar cell parameters in: Proceedings of the IEEE 38th Photovoltaic Specialists Conference (PVSC), Austin, TX, USA, IEEE, 2012, pp. 1855-1859.

[2] M. Glatthaar, J. Haunschild, R. Eidler, M. Demant, J. Greulich, B. Michl, W. Warta, S. Rein, R. Preu, Evaluating luminescence based voltage images of silicon solar cells, J. Appl. Phys. 108 (2010) 014501.
[3] O. Breitenstein, Local efficiency analysis of solar cells based on lock-in thermography, Sol. Energy Mater. Sol. Cells 107 (2012) 381–389.
[4] C. Shen, H. Kampwerth, M.A. Green, T. Trupke, J. Carstensen, A. Schütt, Spatially resolved photoluminescence imaging of essential silicon solar cell parameters and comparison with CELLO measurements, Sol. Energy Mater. Sol. Cells 109 (2013) 77–81.
[5] J. Carstensen, A. Schütt, H. Föll, CELLO local solar cell resistance maps: modeling of data and correlation to solar cell efficiency, in: Proceedings of the 22nd European Photovoltaic Solar Energy Conference, 1CV.1.34, Milan, 2007.
[6] O. Breitenstein, C. Shen, H. Kampwerth, M.A. Green, Comparison of DLIT- and PL-based local solar cell efficiency Analysis, in: Contribution at Third International Conference on Crystalline Silicon Photovoltaics "SiliconPV 2013", Hamelin, Germany, 2013.
[7] T. Trupke, E. Pink, R.A. Bardos, M.D. Abbott, Spatially resolved series resistance of silicon solar cells obtained from luminescence imaging, Appl. Phys. Lett. 90 (2007) 93506.
[8] T. Fuyuki, H. Kondo, T. Yamazaki, Y. Takahashi, Y. Uraoka, Photographic surveying of minority carrier diffusion length in polycrystalline silicon solar cells by electroluminescence, Appl. Phys. Lett. 86 (2005) 262108.
[9] S.R. Wenham, M.A. Green, M.E. Watt, R. Corkish, Applied Photovoltaics, second edition, 37 (ISBN 978-0-7334-2734-3).
[10] S. Rißland, O. Breitenstein, Evaluation of luminescence images of solar cells for injection-level dependent lifetimes, Sol. Energy Mater. Sol. Cells 111 (2013) 112–114.
[11] BT imaging Pty Ltd ⟨www.btimaging.com⟩.
[12] H. Kampwerth, T. Trupke, J.W. Weber, Y. Augarten, Advanced luminescence based effective series resistance imaging of silicon solar cells, Appl. Phys. Lett. 93 (2008) 202102.
[13] M. Kasemann, D. Grote, M. Kasemann, D. Grote, B. Walter, W. Kwapil, T. Trupke, Y. Augarten, R.A. Bardos, E. Pink, M.D. Abbott, W. Warta, Luminescence imaging for the detection of shunts on silicon solar cells, Prog. Photovolt.: Res. Appl. 16 (2008) 297–305.
[14] O. Breitenstein, S. Rissland, A two-diode model regarding the distributed series resistance, Sol. Energy Mater. Sol. Cells 110 (2013) 77–86.
[15] J. Wong, Perturbation theory for solar cell efficiency II – delineating series resistance, IEEE Trans. Electron Devices 60 (3) (2013) 917–922.
[16] G.L. Araújo, A. Cuevas, J.M. Ruiz, The effect of distributed series resistance on the dark and illuminated current-voltage characteristics of solar cells, IEEE Trans. Electron Devices 33 (1986) 391–401.
[17] O. Breitenstein, S. Rißland, A two-diode model regarding the distributed series resistance, Sol. Energy Mater. Sol. Cells 110 (2013) 77–86.
[18] M. Padilla, B. Michl, B. Thaidigsmann, W. Warta, M.C. Schubert, Short-circuit current density mapping for solar cells, Sol. Energy Mater. Sol. Cells 120 (2013) 282–288.
[19] Z. Hameiri, P. Chaturvedi, K.R. McIntosh, Imaging the local ideality factor by contactless photoluminescence measurement, Appl. Phys. Lett. 103 (2013) 023501.